Broadband Negative Reflection of Underwater Acoustic Waves from a Simple Metagrating: Modeling and Experiment

Simon Bernard ⬤,[*] Feriel Chikh-Bled, Hasna Kourchi, Farid Chati, and Fernand Léon

Laboratoire Ondes et Milieux Complexes (LOMC), UMR CNRS 6294, Université Le Havre Normandie, 75 rue Bellot, Le Havre 76600, France

Metagratings are periodic arrays of subwavelength scatterers, or atoms, engineered to refract or reflect waves toward anomalous directions with unit efficiency. Here, we design and build a metagrating to control the reflection direction of waterborne ultrasound waves impinging on a rigid or free surface. The grating and its atoms are designed to cancel the specular reflection and to redirect acoustic power toward a negative-reflection direction, through the first-negative-order Floquet mode. Despite a simple design, based on C-shaped brass particles acting as Helmholtz resonators, the grating is efficient ($> 90\%$) over a relatively broad range of frequencies (74–103 kHz) for a broad range of incidence angles ($14°$–$54°$). This good performance is obtained by tuning the distance between the atoms and the reflective surface. A multiple-scattering analytical model is presented to explain the phenomenon and a finite-element model is developed to further investigate the performance of the proposed design. Predictions from the model are confirmed experimentally in a water tank. The simplicity, reconfigurability, and scalability of the design, as well as its high efficiency, broadband behavior, and robustness to the incidence angle are all features that make the grating potentially useful for various applications in underwater acoustics, such as telemetry, communication, or noise mitigation.

I. INTRODUCTION

Bulk three-dimensional (3D) metamaterials and thin two-dimensional (2D) metasurfaces are designed to offer extraordinary wave-propagation properties, usually from an assembly of multiple subwavelength elements. Many metasurfaces have been developed in recent years, both for electromagnetic waves [1–5] and acoustic waves [6–9]. One application of metasurfaces is to redirect waves toward anomalous directions not classically allowed by the reflection and refraction laws [10–13]. This can be achieved using a phase-gradient metasurface: a local phase shift is applied by the surface to modify the momentum of the wave and reroute it toward the desired direction, according to the so-called generalized Snell-Descartes laws [14]. The phase gradient can be discretized by engineering multiple small elements, or atoms, to offer the desired local phase shift. In acoustics, space-coiling structures or Helmholtz-like resonators are often employed [7] but require tedious design and precise manufacturing. In air acoustics, 3D printing can provide complex structures quickly and at low cost but most 3D-printing materials are inappropriate for underwater applications because of a low contrast in acoustic impedance. Furthermore, such surfaces usually work optimally in a narrow frequency band,

as complex meta-atoms will only offer the desired phase response at their design wavelength. Recent works have highlighted another limitation: even with a perfect realization of the phase gradient, the efficiency is intrinsically limited for large steering angles [15,16]. This can be overcome by designing locally active or nonlocal metasurfaces, relying on near-field coupling between the atoms [16,17]. However, this comes at the cost of further increased design and fabrication challenges.

The concept of the metagrating relies on a different physical principle and on a simpler design based on a periodic cell containing down to one single atom [18–25]. The possible outgoing wave directions are governed by the periodicity (Fig. 1). By engineering the atoms, the unwanted diffraction channels can be suppressed and all the impinging energy rerouted to a desired direction with unitary efficiency [18,20]. Such gratings have been recently demonstrated experimentally for acoustics in air [25] and numerically for underwater acoustics [24]. Another benefit over phase-gradient metasurfaces is the existence of configurations that are effective over a large bandwidth and a large range of incidence angles, as recently demonstrated in optics [26–28] and in this study for acoustics.

Resonant atoms can provide the desired scattering properties [18]. Here, we use C-shaped atoms, which behave as Helmholtz resonators with a low-frequency resonance

---

*simon.bernard@univ-lehavre.fr
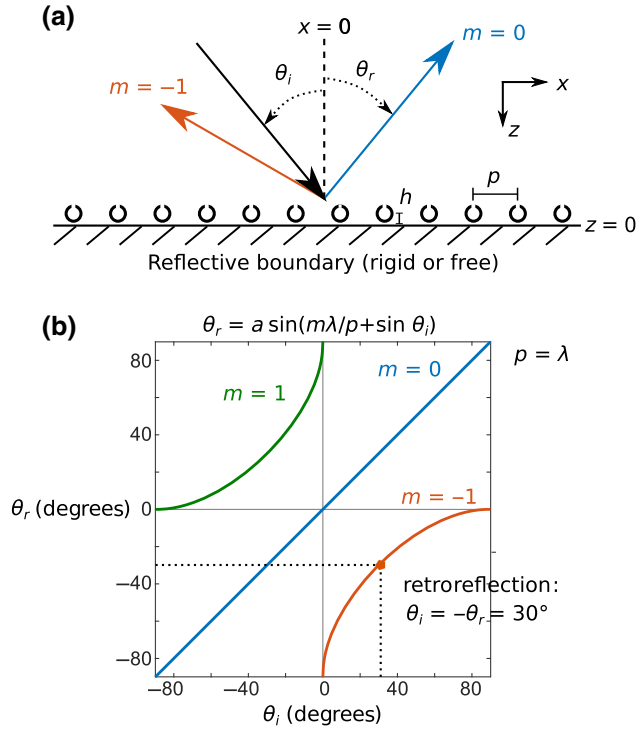
(a)

(b)

FIG. 1. (a) To achieve anomalous reflection, metagratings rely on periodicity, which allows only a finite number of reflected modes to exist, given by the grating equation, illustrated in (b) for $p = \lambda$. By tailoring the scattering properties of the atoms, the $m = 0$ mode and the specular reflection from the surface behind the grating can be tuned to cancel each other, so that all the energy is rerouted toward the desired anomalous direction.

mainly governed by the size of the cavity and neck opening. Such atoms have recently attracted interest in acoustic wave manipulation, as they are easy to fabricate and offer interesting scattering properties [25,29]. In this study, we design and build a metagrating for anomalous reflection of underwater ultrasound waves around 90 kHz, from small (radius approximately $\lambda/6$) brass atoms, with a focus on negative reflection: the goal is to redirect the incoming energy toward the direction of the incident wave. We demonstrate how, by adequately choosing the distance between the grating and the reflective surface, it is possible to obtain near-unit efficiency over a large frequency band and range of incidence angles. The broadband and broadangle effects are linked to the multiple scattering of the wave by the surface and the atoms and an analytical model is provided, as well as finite-element modeling (FEM) and an experimental demonstration.

II. ANALYTICAL MODEL AND PARAMETER SELECTION

Consider a periodic grating of small atoms located at a height h from a perfectly reflecting surface. The surface

can be either an acoustic free (acoustic pressure = 0) or a rigid (normal velocity = 0) boundary condition. When the grating is illuminated by a plane acoustic wave with incidence angle θ_i, only a finite number of reflected plane waves, or Floquet modes, can exist. Their reflection angles θ_r are related to the periodicity p and wavelength λ by the grating equation [30,31]:

$$\sin(\theta_r) - \sin(\theta_i) = m\frac{\lambda}{p}, \tag{1}$$

where m is an integer. Solutions of Eq. (1) are plotted in Fig. 1(b) for $p = \lambda$. In this case, three reflection channels exist: $m = 0$, for which $\theta_r = \theta_i$ for all θ_i, and the $m = -1$ and $m = 1$ modes, which exist, respectively, for $\theta_i > 0$ and $\theta_i < 0$. With these parameters, $\theta_i = 30°$ corresponds to the case of retroreflection, where the $m = -1$ mode is reflected exactly toward the direction of the incoming wave. When two or more channels coexist at a given incidence angle, their relative weight depends on the scattering properties of the atoms [18]. The goal is to tune the scattering such that the weight of one selected mode is made as close as possible to 1, while other unwanted modes are close to 0. In this study, we focus on negative reflection: in the range of parameters for which the $m = 0$ and $m = -1$ modes exists, we design the grating such that the $m = 0$ mode cancels the specular reflection from the surface behind the grating, so that all energy is reflected by the $m = -1$ channel, in a negative direction as shown in Fig. 1(a).

Under a monopolar scattering approximation, which is valid for small atoms, the $m = 0$ mode exactly cancels the specular reflection if, for the rigid boundary condition (see the Appendix),

$$\frac{1}{\alpha} = \frac{2i}{p}\frac{\omega c}{\cos\theta_i}\cos^2(kh\cos\theta_i), \tag{2}$$

and for the free-boundary condition,

$$\frac{1}{\alpha} = \frac{-2i}{p}\frac{\omega c}{\cos\theta_i}\sin^2(kh\cos\theta_i), \tag{3}$$

where α is the effective monopolar polarizability of an atom and $k = 2\pi/\lambda = 2\pi f/c$. We see in both cases that α must be purely imaginary, which happens at the metagrating resonance [18,32]. Note that α is the *effective* polarizability of an atom, defined in the presence of all other atoms and a reflective surface. Furthermore, in order to perfectly match the power of the incident wave to the power radiated through the $m = -1$ channel, we need to satisfy [18] (see also the Appendix):

$$\frac{1}{\cos\theta_i}\cos^2(kh\cos\theta_i) = \frac{1}{\cos\theta_r}\cos^2(kh\cos\theta_r) \tag{4}$$

for the rigid boundary condition, and

$$\frac{1}{\cos \theta_i} \sin^2(kh \cos \theta_i) = \frac{1}{\cos \theta_r} \sin^2(kh \cos \theta_r) \quad (5)$$

for the free-boundary condition. We see, as noted by Ra'di *et al.* [18], that retroreflection ($\theta_r = -\theta_i$) is a trivial solution of these equations, meaning that it can be obtained whatever the distance h. However, as we now show, the solution is more robust to a change in wavelength or angle for some values of h, providing a broadband and broad-angle behavior.

We define ϵ as the ratio of the left-hand to the right-hand term in Eqs. (4) or (5). By considering wave scattering by the grating and its *virtual* conterpart on the other side of the reflective surface, we can arrive at (see the Appendix)

$$\epsilon = \frac{\cos \theta_r}{\cos \theta_i} \frac{\cos^2(kh \cos \theta_i)}{\cos^2(kh \cos \theta_r)} \quad (6)$$

for the rigid boundary condition, and

$$\epsilon = \frac{\cos \theta_r}{\cos \theta_i} \frac{\sin^2(kh \cos \theta_i)}{\sin^2(kh \cos \theta_r)} \quad (7)$$

for the acoustic free boundary. We plot ϵ as a function of h and the incident wave frequency f in Fig. 2 for both boundary conditions, for $\theta_i = 30°$, $c = 1470$ m/s and $p = \lambda = 17$ mm [and using the grating equation Eq. (1), to obtain θ_r as a function of f]. In addition to the trivial solution ($\theta_r = -\theta_i$), corresponding to the vertical white lines at about 87 kHz that are visible in Figs. 2(a) and 2(b), other solution branches exist. In the rigid case, for $h = 8$ mm, we observe a large valley of near unity ϵ, due to a solution branch crossing the $\theta_r = -\theta_i$ solution. In this region, the metagrating is able to efficiently couple the incoming power to the $m = -1$ channel over a broad range of frequencies, through complex wave interactions between the grating and the reflective surface. In the free-boundary case, two interesting values of h exist: h very small, with the minimal values in practice being equal to the radius of the atoms (2.5 mm here; see below) or $h = 13$ mm.
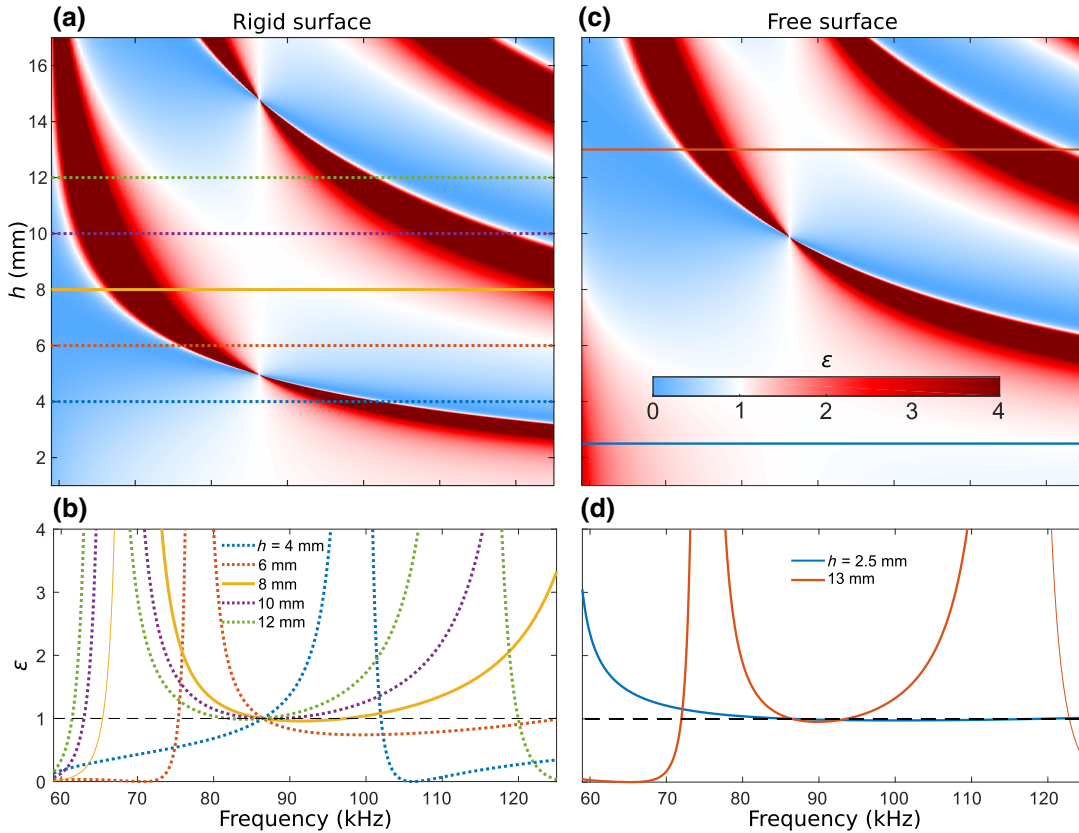

FIG. 2. Tuning the distance h between the grating and the rigid (a),(b) or free (c),(d) reflective surface. ϵ is the ratio of the left-hand to the right-hand term in Eqs. (4) or (5). A value of 1 (white) satisfies the conditions for anomalous reflection with unitary efficiency. The vertical white line at 87 kHz is the trivial solution $\theta_r = -\theta_i$. For $h = 8$ mm for the rigid surface, ϵ is close to 1 over a broad range of frequencies, particularly in the range [80–105] kHz. For the free surface, two interesting solutions exist: $h = 13$ mm and h close to 0 (the smallest possible value in practice being equal to the radius of the atom).

The dispersion relation between the wavelength and reflective angle [Eq. (1)] implies that if the specular reflection is canceled over a broad frequency range, the energy is reflected toward a varying angle. Consequently, a broadband wave cannot be redirected to a given direction. This is a limitation of the metagrating. On the other hand, we can also observe that the reflective and incidence angles play symmetric roles in Eqs. (4) and (5), implying that the broadband behavior is associated with robustness with respect to the incidence angle.

III. FINITE-ELEMENT MODELING OF THE PERIODIC GRATING

A FE model of the periodic metagrating is built using COMSOL MULTIPHYSICS. The acoustic structure interaction module is used to take into account the elastic nature of the atoms. The geometry and material properties are set according to the actual grating (see Sec. IV). The wave velocity and the mass density of water are 1470 m/s and 1000 kg/m³, respectively. Modeling is done in the frequency domain. A single periodic cell of the grating is modeled as a rectangular box, using Floquet periodic boundary conditions to obtain the behavior of an infinite grating. A rigid (normal velocity = 0) or free (acoustic pressure = 0) boundary condition is set behind the atoms and a matched boundary condition at the opposite boundary is set to perfectly absorb the $m = 0$ and $m = -1$ reflected modes. The incident wave is a planar wave background pressure field with unit amplitude. The power radiated by each of the possible propagation modes is evaluated by integration over the opposite boundary and expressed as the (quadratic) reflection coefficient $|R_m|^2$.

The results of the FEM modeling of the periodic grating for the rigid boundary case for $h = 8$ mm are presented in Fig. 3. Figure 3(a) displays the reflection coefficient of the anomalous reflection $m = -1$ for all incidence angles from $0°$ to $90°$. The efficiency remains excellent (> 0.9) for a broad range of incidence angles ($14°$ to $54°$) around the design angle of $30°$. The bandwidth is shrinking for extreme angles but is still reasonably large for angles from about $20°$ to $40°$. The reflection angle here depends on both the incidence angle and the frequency, according to Eq. (1). Retroreflection ($\theta_r = -\theta_i$) is achieved along the purple line. More than 50% of the incoming power can be retroreflected for frequencies ranging from 65 to 111 kHz and angles from $23°$ to $43°$. The sharp bright lines in panel (a) correspond to the appearance of new possible reflection modes among $m = -2$, $m = -1$, and $m = 1$. The reflection coefficients of each channel are plotted in panel (b) for $\theta_i = 30°$. Up to 115 kHz, only the $m = 0$ and $m = -1$ modes exist, in agreement with Eq. (1). Above 70 kHz, the $m = -1$ reflection mode becomes dominant, up to 108 kHz. Between 74 kHz and 103 kHz, more than 90% of the power is directed toward the anomalous reflection
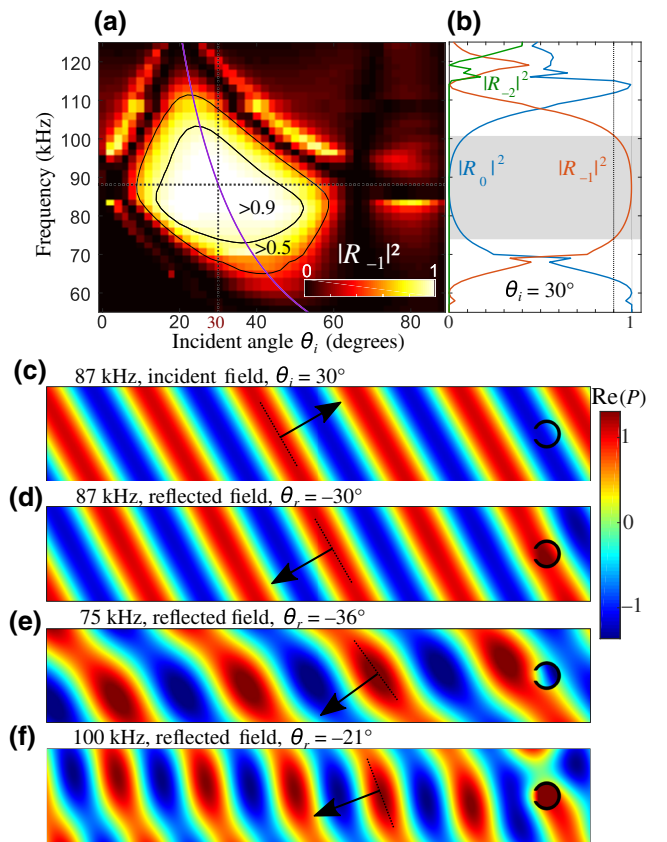

FIG. 3. The FEM results for the proposed metagrating over a rigid surface with height $h = 8$ mm. (a) The reflection coefficient of the anomalous reflection ($m = -1$) channel as a function of the incidence angle and frequency. The purple line indicates retroreflection ($\theta_r = -\theta_i$). (b) The reflection coefficient of the channels $m = 0$ (specular), $m = -1$, and $m = -2$ for $\theta_i = 30°$. The bandwidth over which $|R_{-1}| > 0.9$ is highlighted in gray. (c)–(f) Maps of the incident (c) or reflected (d)–(f) acoustic pressure field. At 87 kHz, the retroreflection is perfect. At 75 kHz and 100 kHz, the anomalous reflection is less than perfect but still efficient.

direction, demonstrating near-unit efficiency over a large bandwidth (approximately 1/3 of the central frequency). Panels (c) and (d) show, respectively, the incident and reflected wave fields (the real part of the acoustic pressure) at 87 kHz ($p = \lambda$) for $\theta_i = 30°$. In this case retroreflection is perfect, with efficiency > 0.998. At 75 kHz and 100 kHz [Figs. 3(e) and 3(f)], the anomalous reflection is less than perfect, as is visible from the slightly distorted wave fronts, but remains efficient.

Similar results are displayed in Fig. 4 for the free-boundary case, for height $h = 13$ mm and $h = 2.5$ mm, respectively, in Figs. 4(a)–4(d). For $h = 13$ mm, the observed effect is qualitatively similar to the effect observed for $h = 8$ mm for the rigid boundary. This is not surprising, as in both cases the broadband effect is due to a crossing of two solution branches of the equation $\epsilon = 0$ in
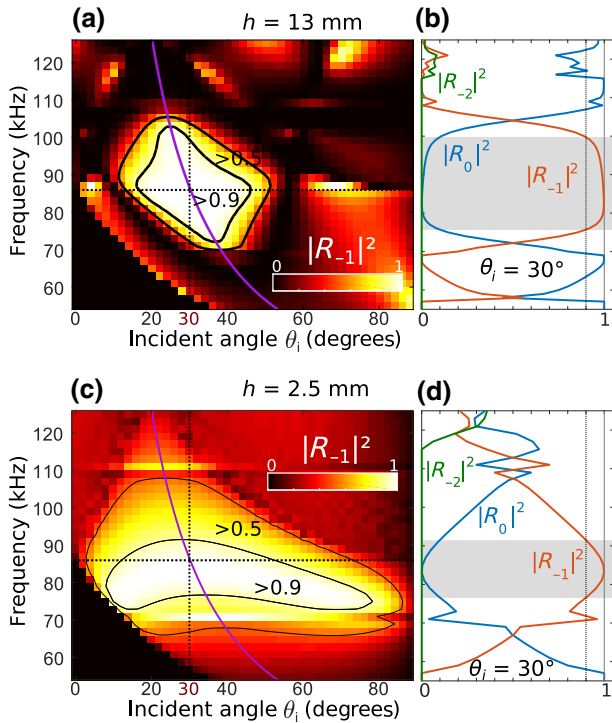
FIG. 4. The FEM results for an acoustic free surface, with height $h = 13$ mm (a),(b) and $h = 2.5$ mm (c),(d). Maps (a) and (c) show the reflection coefficient of the anomalous reflection ($m = -1$) channel as a function of the incidence angle and frequency. The purple line indicates retroreflection ($\theta_r = -\theta_i$). Plots (b) and (d) show the reflection coefficient of the channels $m = 0$ (specular), $m = -1$, and $m = -2$ for $\theta_i = 30°$. The bandwidth over which $|R_{-1}| > 0.9$ is highlighted in gray.

the frequency-distance h space (Fig. 2). For $h = 2.5$ mm, the effect is qualitatively different: the range of incidence angle over which the efficiency is > 0.9 is even larger, spanning from $10°$ to $78°$. The grating is therefore highly efficient from near normal to very grazing incidence. The frequency band of high efficiency is somewhat narrower in this case but the decrease in efficiency when moving away from the design frequency is less sharp than in the previous cases and the grating still has > 0.5 efficiency on a reasonably broad band (67–107 kHz at $30°$ incidence).

IV. EXPERIMENTAL DEMONSTRATION WITH A RIGID SURFACE

Experimentally, the atoms making up the metagrating are made from 300-mm-long hollow brass cylinders, with external radius $r_{ext} = 2.50$ mm and internal radius $r_{in} = 2.05$ mm. They are opened on one side using a milling cutter to form C-shaped atoms (see Fig. 5). The opening is $\delta = 2$ mm large, forming a Helmholtz resonator with a broad resonance at about 90 kHz. Brass is selected because (1) it can be found easily in the desired shape at low cost, (2) it is resistant to corrosion, even when immersed in
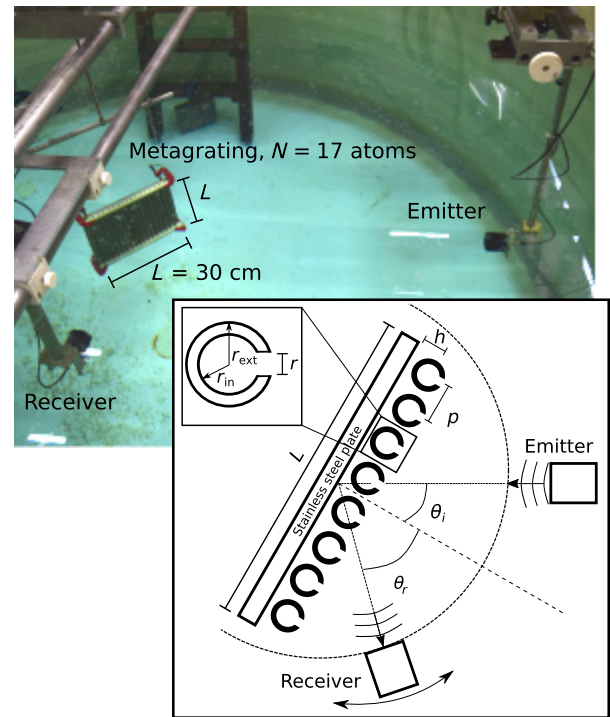

FIG. 5. A photograph and schematic of the experimental setup. The target can be rotated to vary the incidence angle, while the receiving angle can also be modified. The design parameters of the atom and grating are given in the text.

water for several consecutive days, (3) it can be easily milled (as compared to stainless steel), and (4) it is stiff ($E = 100$ GPa) and heavy ($\rho = 8500$ kg/m^3), providing a large acoustic impedance contrast with water. A pairs of PVC blocks are drilled to the desired periodicity $p = 17$ mm (approximately λ at 87 kHz) to assemble the grating from 17 atoms. The structure is then attached in front of a 10-mm-thick stainless steel plate ($L = 300$ by 300 mm) acting as an almost perfect reflector for ultrasound waves in the frequency range of interest. The distance between the center of the tubes and the plate is set to $h = 8$ mm, according to the above analysis.

The experiments are conducted in a water tank (diameter 3 m, height 1.5 m). Two identical ultrasonic transducers are used (Panametrics V3052, central frequency 100 kHz, diameter 38 mm) for transmission and reception. Both transducers are located at about 0.9 m from the bottom of the tank. The distance from the center, where the target (grating plus stainless steel plate) is suspended on a rotating stage, is about 1.4 m for the emitter and 0.4 m for the receiver, respectively. The setup is presented in Fig. 5. A pulser-receiver (Panametrics 5052R) is used to generate a broadband input signal. The received signal is recorded on a digital oscilloscope (Teledyne Lecroy HDO6034). The receiving transducer is rotated through
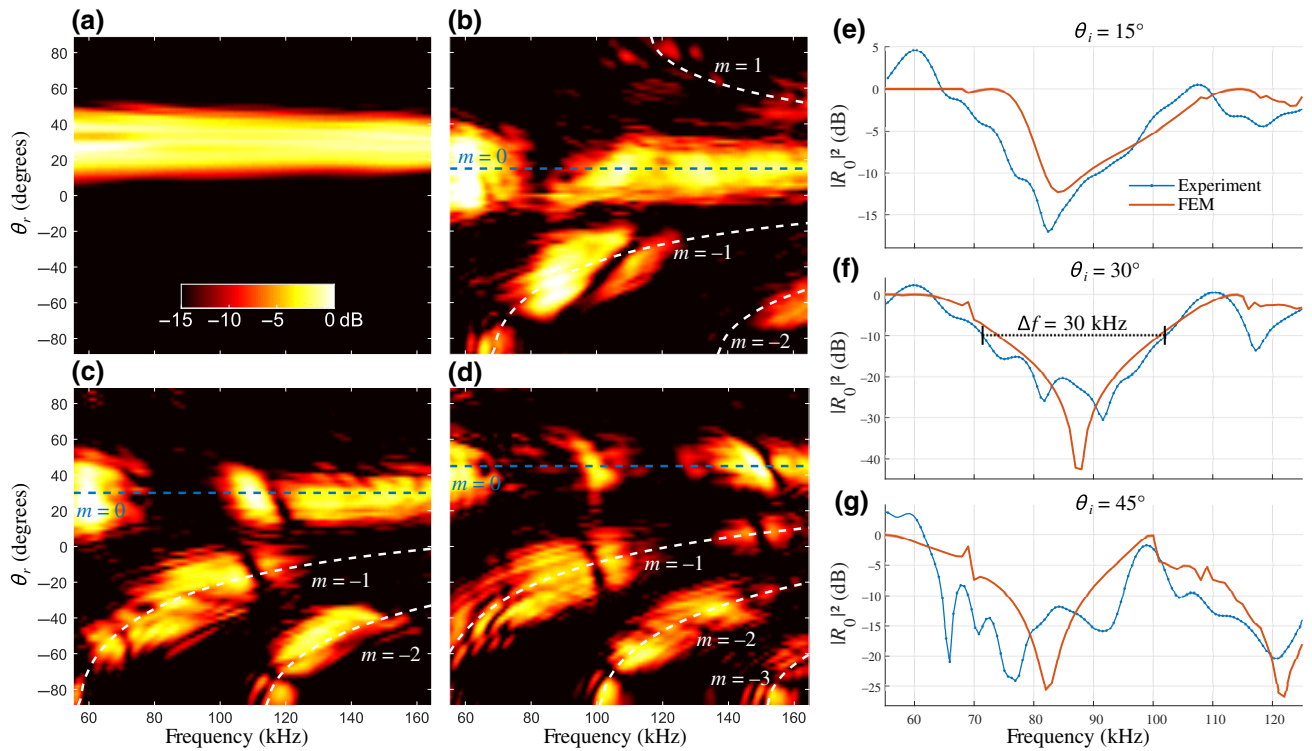
FIG. 6. Experimental results for the constructed metagrating. (a) The amplitude of the reflected pressure wave without a grating (calibration, $\theta_i = 30°$). (b)–(d) The acoustic pressure reflected by the grating for three incidence angles (15°, 30°, and 45°). (e)–(g) Profiles along the specular direction $m = 0$ and a comparison with the FEM results. For $\theta_i = 30°$, the $m = 0$ mode is reduced by more than 10 dB over a broad frequency range (approximately 30 kHz). The surface is still effective for $\theta_i = 15°$ and 45°.

180° in front of the plate, with steps of 2°. For each receiving position, 100 recordings are averaged to improve the signal-to-noise ratio. Time windowing is applied to isolate the reflection on the grating from reflections on the tank boundary and water surface. The spectrum is obtained from a fast Fourier transform and frequency-band correction is applied using the spectrum of the specular reflection on the steel plate alone. The experiment is repeated for three incidence angles (15°, 30°, and 45°).

The experimentally recorded reflected pressure is displayed as a function of the receiving angle and frequency in Figs. 6(a)–6(d). From Fig. 6(a) (no grating, plate only), we can see that the incoming beam contains energy on relatively broad range of angles, from about $\theta_i - 15°$ to $\theta_i + 15°$, due to the finite size of the source. After source-signal spectrum correction, the pressure level is homogeneous from 55 kHz to 165 kHz. In Figs. 6(b)–6(d), we can see how the acoustic power is redirected toward the various modes allowed by the grating equation [Eq. (1)]. The reflected amplitude in the specular ($m = 0$) direction is dramatically reduced in the operating bandwidth of the metagrating [Figs. 6(e)–6(g)], particularly for $\theta_i = 30°$. The experiments are also compared to the FEM prediction in panels (e)–(g). At $\theta_i = 30°$, a reduction down to 30 dB (power divided by 1000) can be observed and the

effective bandwidth at −10 dB (the power divided by ten or 90% efficiency) is about 30 kHz, experimentally confirming the broad bandwidth of the designed grating. The broad-angle behavior is confirmed in Fig. 6(c) by the fact that, for $\theta_i = 30°$, the broad acoustic beam is totally canceled in the specular direction and by the good efficiency observed for $\theta_i = 15°$ and $\theta_i = 45°$ in Figs. 6(b)–6(g). We can also observe narrow gaps in the reflected mode spectra, at frequencies corresponding to the appearance of an additional mode, which are the acoustic analog of Wood's anomaly [33,34], discussion of which is beyond the scope of the present work.

Figure 7 provides an alternative representation of the experimentally recorded pressure at 87 kHz, at which the metagrating is the most effective, for the same four cases: (a) no metagrating and (b)–(d) with the metagrating for incidence angles 15°, 30°, and 45°, respectively. The negative-reflection effect is clearly visible, as in all three cases with the grating, most of the wave pressure is reflected backward, toward the quadrant containing the incident wave vector. The pressure amplitude increases compared to specular reflection pressure for large negative-reflection angles [panel (b)] and decreases for small negative-reflection angles [panel (d)]. This is expected, as a consequence of energy balance: the power
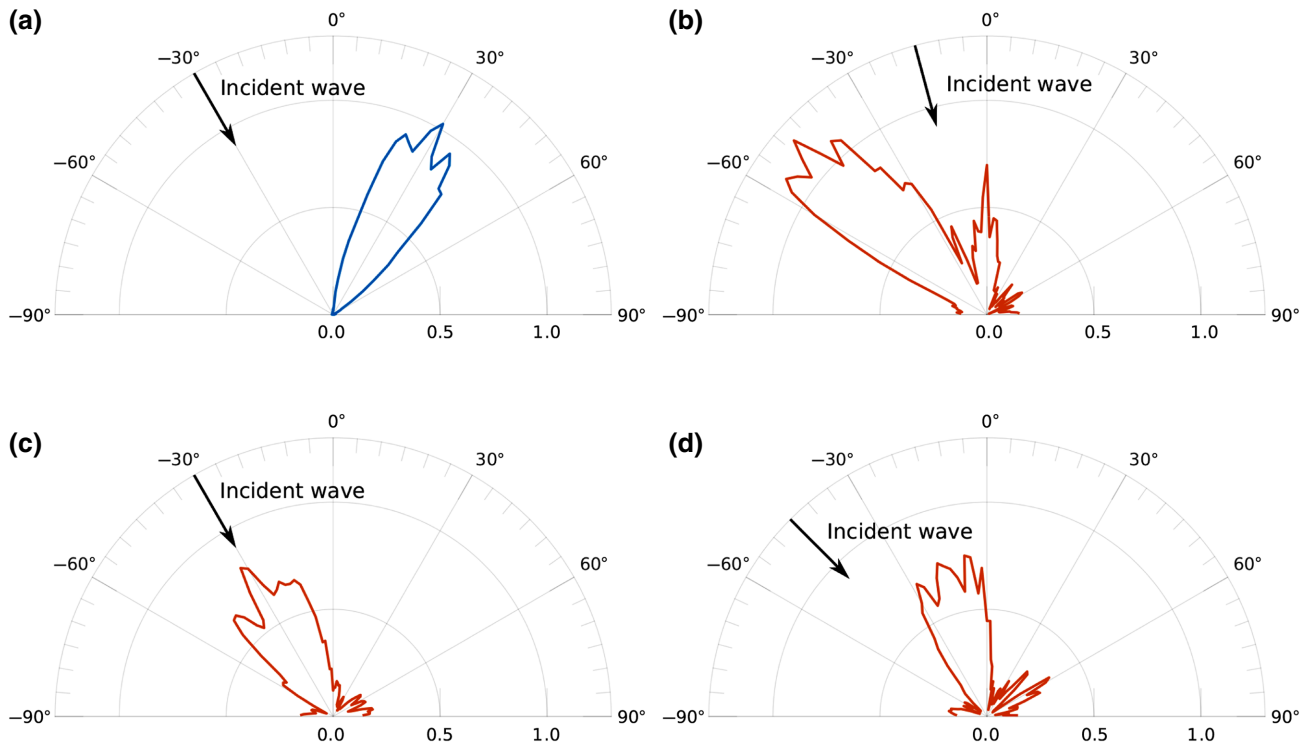
FIG. 7. Polar plots of the reflected pressure at 87 kHz, at which the grating is the most effective: (a) without the metagrating ($\theta_i = 30°$) and (b)–(d) with the metagrating for incidence angles 15°, 30°, and 45°, respectively. The direction of the incident wave is displayed as a black arrow. The amplitudes are normalized to the amplitude of the specular reflection at 30°.

carried away by the anomalous reflection mode is proportional to the product of the acoustic pressure and the cosine of the reflection angle [see Eqs. (A16) and (A17) in the Appendix]. For 30° incidence angle [panel (c)], the amplitude should be expected to be equal to the specular reflection pressure [panel (a)] but is slightly lower. This is an artifact due to our experimental system: at −30° reflection angle (perfect retroreflection), the receiver is located in front of the acoustic source, actually reducing the amount of incident energy.

V. DISCUSSION AND CONCLUSIONS

In this work, we design a metagrating for negative reflection of underwater acoustic waves. This metagrating can operate in front of either a rigid or an acoustic free surface. A detailed analysis of multiple wave scattering between the grating and the surface is presented. This analysis shows that the height h of the grating above the surface is a critical parameter regarding performance. FEM confirms that, once an appropriate value for h has been selected, the negative reflection toward the $m = -1$ Floquet mode can be highly efficient (> 0.9) over a relatively broad frequency range and for a broad range of incidence angles. This is finally verified experimentally in a water tank for the rigid surface, using a metagrating built from C-shaped brass tubes.

The broadband efficiency and simple design are significant steps toward real-world applications in underwater acoustics, where the most commonly encountered acoustic signals, from sonar to noise pollution, are broadband. The fabrication of acoustic metasurfaces is more challenging for water or waterlike media than for air, since stiff and heavy materials are required to provide a large impedance contrast. We demonstrate here that a simple hollow brass cylinder opened at the side is a viable structure for underwater applications. The broadband and broad-angle high efficiency in retroreflection could be useful for telemetry applications based on pulse-echo methods. The relation between the reflection angle and frequency could be used as a benefit to perform real-time processing operations such as, e.g., filtering, frequency discrimination (i.e., spectroscopy) or multiplexing and/or demultiplexing in underwater acoustic communications. The use as a noise barrier can also be envisaged in shallow water, where low-frequency propagation is governed by guided modes reflecting back and forth between the water surface and the ocean bottom at grazing angles. A metagrating, placed close to the water surface, could have the ability to send waves back toward the source or toward the sea bottom with normal incidence, effectively blocking propagation. The design can be scaled to other frequencies and applied to a free boundary. All analytical and numerical

calculations are done under a linear acoustic propagation and linear elasticity assumption, which corresponds to the presented experimental conditions. Extremely high acoustic pressure levels may alter the behavior of the grating, by modifying the resonant behavior of the structure or through nonlinear interactions of multiple scattered waves. This is not investigated here.

In naval applications, one usually seeks to reduce the acoustic power reflected back to the source by a target, which is precisely the opposite of what is achieved here. Further research is needed to develop other configurations, e.g., redirecting a normally incident wave toward a grazing direction. The use of several atoms per period [20,24] could potentially address this challenge. Finally, C-shaped atoms are known to provide strong Willis coupling [35,36], which is not discussed here but could also allow even more challenging wave-control applications by canceling multiple Floquet modes simultaneously.

ACKNOWLEDGMENTS

APPENDIX: ANALYTICAL MODEL OF WAVE DIFFRACTION BY A PERIODIC GRATING CLOSE TO A REFLECTIVE SURFACE

We consider a periodic array of small particles the center of which is at a distance h from a perfectly reflecting surface (either a rigid or a free surface). The configuration is depicted in Fig. 1(a). The surface is aligned with the x axis and at coordinate $z = 0$. The particles are at $z = -h$ and the period is p. An acoustic plane wave of frequency f is incoming from the left, with incidence angle θ_i. The wave velocity and mass density of the propagation medium are c and ρ, respectively.

The incoming pressure wave is

$$p_{\text{inc}} = p_0 e^{i(k_x x + k_z z)}, \quad (A1)$$

with $k_x = k \sin(\theta_i)$, $k_z = k \cos(\theta_i)$ and $k = \omega/c = 2\pi f/c = 2\pi/\lambda$. The pressure wave reflected at the boundary (in the absence of a grating) is

$$p_{\text{ref}}^{\text{rigid-free}} = \pm p_0 e^{i(k_x x - k_z z)}, \quad (A2)$$

where the plus sign $(+)$ is for the rigid case and the minus sign $(-)$ is for the free boundary. Under a monopolar approximation (valid for small particles), the field

scattered by the infinite array of particles is

$$p_{\text{scat}}^{\text{rigid-free}} = A_0 \sum_{n=-\infty}^{+\infty} \left(H_0^1 \left[k\sqrt{(x - np)^2 + (z + h)^2} \right] \right.$$
$$\left. \pm H_0^1 \left[k\sqrt{(x - np)^2 + (z - h)^2} \right] \right) e^{in\phi}, \quad (A3)$$

where H_0^1 is the zero-order Hankel function of the first kind and $\phi = 2\pi p \sin(\theta_i)/\lambda$ is a phase-shift term related to the oblique incidence. The first term in the infinite sum is for the actual particles and the second term is for the "virtual" particles located on the other side of the perfectly reflecting surface. The Poisson summation formula is then used to transform the above sum over an infinite number of particles to a sum over an infinite number of Floquet modes [32]. For the rigid boundary, we obtain

$$p_{\text{scat}}^{\text{rigid}} = \frac{4A_0}{p} \sum_{m=-\infty}^{+\infty} \exp^{i\left(\frac{2\pi m + \phi}{p} x - k_{zm} z\right)}$$
$$\times \frac{\cos(k_{zm} h)}{k_{zm}}, \quad \text{for } z < -h, \quad (A4)$$

and for the free boundary, we obtain

$$p_{\text{scat}}^{\text{free}} = \frac{-4iA_0}{p} \sum_{m=-\infty}^{+\infty} \exp^{i\left(\frac{2\pi m + \phi}{p} x - k_{zm} z\right)}$$
$$\times \frac{\sin(k_{zm} h)}{k_{zm}}, \quad \text{for } z < -h, \quad (A5)$$

where $k_{zm} = \sqrt{k^2 - [(2\pi m + \phi)/p]^2}$ the horizontal wave number for the mth mode. The Floquet modes in the above sums are propagating if k_{zm} is real and are evanescent if k_{zm} is complex. Propagating modes leave the surface with an angle θ_r^m, given by the relation $k \sin(\theta_r^m) = (2\pi m + \phi)/p$, from which we can arrive at the grating equation $\sin(\theta_r^m) - \sin(\theta_i) = m\lambda/p$.

To achieve perfect anomalous reflection, i.e., having the incident wave redirected with unit efficiency into a single plane wave the angle of which can be controlled, we need two propagating Floquet modes: one being the controlled reflected wave and the other canceling the specular reflection. One of these two modes is necessarily the mode $m = 0$, as $k_{z0} = k_z$ is real. The second can be either $m = 1$ or $m = -1$, depending on the sign of θ_i. We assume here that $\theta_i > 0$, in which case we need the modes $m = 0$ and $m = -1$ to be propagating and all others to be evanescent. A mode m is evanescent if $\sin(\theta_r^m) - \sin(\theta_i) = m\lambda/p$ has no solution. For $m = 1$, no solution exists if $p < \lambda/(1 - \sin\theta_i)$. Satisfying this condition also ensures that modes $m = 2, 3, \ldots$ are evanescent. For $m = -2$ to be evanescent (and also $m = -3, -4, \ldots$), we arrive at the

condition $p < 2\lambda/(1 + \sin\theta_i)$. For $p = \lambda$, both conditions are satisfied for all angles $\theta_i > 0$.

The total wave field is then $p_{\text{tot}} = p_{\text{inc}} + p_{\text{ref}} + p_{m=0} + p_{m=-1}$, which leads to, for the rigid boundary,

$$p_{\text{tot}} = p_0 e^{i(k_x x + k_z z)} + p_0 e^{i(k_x x - k_z z)} + \frac{4A_0}{p} e^{i(k_x x - k_z z)} \frac{\cos(k_z h)}{k_z}$$
$$+ \frac{4A_0}{p} e^{i[k\sin(\theta_r^{-1})x - k\cos(\theta_r^{-1})z]} \frac{\cos[k\cos(\theta_r^{-1})h]}{k\cos(\theta_r^{-1})}, \tag{A6}$$

where $k\sin(\theta_r^{-1}) = (\phi - 2\pi)/p$ and $k\cos(\theta_r^{-1}) = \sqrt{k^2 - [(\phi - 2\pi)/p]^2}$. For the free boundary, we arrive at

$$p_{\text{tot}} = p_0 e^{i(k_x x + k_z z)} - p_0 e^{i(k_x x - k_z z)} - \frac{4iA_0}{p} e^{i(k_x x - k_z z)} \frac{\sin(k_z h)}{k_z}$$
$$- \frac{4iA_0}{p} e^{i[k\sin(\theta_r^{-1})x - k\cos(\theta_r^{-1})z]} \frac{\sin[k\cos(\theta_r^{-1})h]}{k\cos(\theta_r^{-1})}. \tag{A7}$$

For the $m = 0$ mode to cancel the specular reflection, it is therefore required that

$$p_0 = \frac{-4A_0}{p} \frac{\cos(k_z h)}{k_z} \tag{A8}$$

for the rigid boundary and that

$$p_0 = \frac{-4iA_0}{p} \frac{\sin(k_z h)}{k_z} \tag{A9}$$

for the free boundary. The zero-order scattering coefficient A_0 is related to the effective monopolar polarizability α of the particle by the relation [36]

$$A_0 = \frac{-ik^2 c^2}{4} \alpha(\tilde{p}_{\text{inc}} + \tilde{p}_{\text{ref}}), \tag{A10}$$

where $\tilde{p}_{\text{inc}}$ and $\tilde{p}_{\text{ref}}$ denote, respectively, the incident and reflected pressure at the center of the particle. For the rigid boundary we have, for a particle located at $x = 0$ and $z = -h$,

$$\tilde{p}_{\text{inc}} + \tilde{p}_{\text{ref}} = p_0 e^{ik_z h} + p_0 e^{-ik_z h} = 2p_0 \cos(k_z h), \tag{A11}$$

and for the free boundary,

$$\tilde{p}_{\text{inc}} + \tilde{p}_{\text{ref}} = p_0 e^{ik_z h} - p_0 e^{-ik_z h} = -2ip_0 \sin(k_z h). \tag{A12}$$

Inserting these equations in Eq. (A10) and satisfying the conditions given in Eqs. (A8) and (A9), we find that

$$\frac{1}{\alpha} = \frac{2i}{p} \frac{\omega c}{\cos\theta_i} \cos^2(kh\cos\theta_i) \tag{A13}$$

for the rigid boundary and

$$\frac{1}{\alpha} = \frac{-2i}{p} \frac{\omega c}{\cos\theta_i} \sin^2(kh\cos\theta_i) \tag{A14}$$

for the free boundary. In both cases, we see that α must be purely imaginary for the $m = 0$ Floquet mode to cancel the specular reflection, which happens at the grating resonance [18,32].

In addition, it is also required for perfect anomalous reflection that the power carried away from the surface by $m = -1$ mode matches the incoming power. The incoming power is equal to

$$P_i = \frac{p_0^2 p}{2\rho c} \cos\theta_i. \tag{A15}$$

The power carried away by the $m = -1$ mode is, now simplifying notation using $\theta_r^{-1} = \theta_r$, for the rigid boundary,

$$P_{m=-1} = \frac{p}{2\rho c} \cos(\theta_r) \left(\frac{4A_0}{p}\right)^2 \frac{\cos^2(kh\cos\theta_r)}{k^2 \cos^2(\theta_r)}, \tag{A16}$$

and for the free boundary,

$$P_{m=-1} = \frac{p}{2\rho c} \cos(\theta_r) \left(\frac{4iA_0}{p}\right)^2 \frac{\sin^2(kh\cos\theta_r)}{k^2 \cos^2(\theta_r)}. \tag{A17}$$

Using the conditions given in Eqs. (A8) and (A9) for p_0 above and equating incident and carried-away powers leads to

$$\frac{1}{\cos\theta_i} \cos^2(kh\cos\theta_i) = \frac{1}{\cos\theta_r} \cos^2(kh\cos\theta_r),$$

for the rigid boundary and
$$\tag{A18}$$

$$\frac{1}{\cos\theta_i} \sin^2(kh\cos\theta_i) = \frac{1}{\cos\theta_r} \sin^2(kh\cos\theta_r),$$

for the free boundary. $\tag{A19}$

Depending on the nature of the reflective surface behind the grating, one of these two last conditions has to be satisfied along the grating resonance condition in order to achieve perfect negative reflection. We can see that retroreflection, $\theta_r = -\theta_i$, is always a solution, for any distance h. However, as demonstrated in the main text, there are other nontrivial solutions and there exist values of h for which the conditions can be approximately satisfied over a broad range of frequencies and incidence angles, leading to a robust broadband negative-reflection effect.

[1] C. L. Holloway, E. F. Kuester, J. A. Gordon, J. O'Hara, J. Booth, and D. R. Smith, An overview of the theory and applications of metasurfaces: The two-dimensional equivalents of metamaterials, IEEE Antennas Propag. Mag. **54,** 10 (2012).

[2] C. Pfeiffer and A. Grbic, Metamaterial Huygens' Surfaces: Tailoring Wave Fronts with Reflectionless Sheets, Phys. Rev. Lett. **110,** 197401 (2013).

[3] N. Yu and F. Capasso, Flat optics with designer metasurfaces, Nat. Mater. **13,** 139 (2014).

[4] Y. Zhao, X.-X. Liu, and A. Alù, Recent advances on optical metasurfaces, J. Opt. **16,** 123001 (2014).

[5] S. B. Glybovski, S. A. Tretyakov, P. A. Belov, Y. S. Kivshar, and C. R. Simovski, Metasurfaces: From microwaves to visible, Phys. Rep. **634,** 1 (2016). metasurfaces: From microwaves to visible

[6] G. Ma and P. Sheng, Acoustic metamaterials: From local resonances to broad horizons, Sci. Adv. **2,** e1501595 (2016).

[7] B. Assouar, B. Liang, Y. Wu, Y. Li, J.-C. Cheng, and Y. Jing, Acoustic metasurfaces, Nat. Rev. Mater. **3,** 460 (2018).

[8] B. Liang, J.-C. Cheng, and C.-W. Qiu, Wavefront manipulation by acoustic metasurfaces: From physics and applications, Nanophotonics **7,** 1191 (2018).

[9] Y. Wu, M. Yang, and P. Sheng, Perspective: Acoustic metamaterials in transition, J. Appl. Phys. **123,** 090901 (2018).

[10] Y. Li, B. Liang, Z.-m. Gu, X.-y. Zou, and J.-c. Cheng, Reflected wavefront manipulation based on ultrathin planar acoustic metasurfaces, Sci. Rep. **3,** 1 (2013).

[11] Y. Li, X. Jiang, R.-q. Li, B. Liang, X.-y. Zou, L.-l. Yin, and J.-c. Cheng, Experimental Realization of Full Control of Reflected Waves with Subwavelength Acoustic Metasurfaces, Phys. Rev. Appl. **2,** 064002 (2014).

[12] J. Mei and Y. Wu, Controllable transmission and total reflection through an impedance-matched acoustic metasurface, New J. Phys. **16,** 123007 (2014).

[13] Y. Xie, W. Wang, H. Chen, A. Konneker, B.-I. Popa, and S. A. Cummer, Wavefront modulation and subwavelength diffractive acoustics with an acoustic metasurface, Nat. Commun. **5,** 1 (2014).

[14] N. Yu, P. Genevet, M. A. Kats, F. Aieta, J.-P. Tetienne, F. Capasso, and Z. Gaburro, Light propagation with phase discontinuities: Generalized laws of reflection and refraction, Science **334,** 333 (2011).

[15] N. M. Estakhri and A. Alu, Wave-Front Transformation with Gradient Metasurfaces, Phys. Rev. X **6,** 041008 (2016).

[16] A. Díaz-Rubio and S. A. Tretyakov, Acoustic metasurfaces for scattering-free anomalous reflection and refraction, Phys. Rev. B **96,** 125409 (2017).

[17] A. Epstein and G. V. Eleftheriades, Synthesis of Passive Lossless Metasurfaces Using Auxiliary Fields for Reflectionless Beam Splitting and Perfect Reflection, Phys. Rev. Lett. **117,** 256103 (2016).

[18] Y. Ra'di, D. L. Sounas, and A. Alù, Metagratings: Beyond the Limits of Graded Metasurfaces for Wave Front Control, Phys. Rev. Lett. **119,** 067404 (2017).

[19] A. Epstein and O. Rabinovich, Unveiling the Properties of Metagratings via a Detailed Analytical Model for Synthesis and Analysis, Phys. Rev. Appl. **8,** 054037 (2017).

[20] D. Torrent, Acoustic anomalous reflectors based on diffraction grating engineering, Phys. Rev. B **98,** 060101(R) (2018).

[21] Z. Hou, X. Fang, Y. Li, and B. Assouar, Highly Efficient Acoustic Metagrating with Strongly Coupled Surface Grooves, Phys. Rev. Appl. **12,** 034021 (2019).

[22] Y. Fu, Y. Cao, and Y. Xu, Multifunctional reflection in acoustic metagratings with simplified design, Appl. Phys. Lett. **114,** 053502 (2019).

[23] H. Ni, X. Fang, Z. Hou, Y. Li, and B. Assouar, High-efficiency anomalous splitter by acoustic meta-grating, Phys. Rev. B **100,** 104104 (2019).

[24] L. Fan and J. Mei, Metagratings for Waterborne Sound: Various Functionalities Enabled by an Efficient Inverse-Design Approach, Phys. Rev. Appl. **14,** 044003 (2020).

[25] Y. K. Chiang, S. Oberst, A. Melnikov, L. Quan, S. Marburg, A. Alù, and D. A. Powell, Reconfigurable Acoustic Metagrating for High-Efficiency Anomalous Reflection, Phys. Rev. Appl. **13,** 064067 (2020).

[26] Z.-L. Deng, S. Zhang, and G. P. Wang, A facile grating approach towards broadband, wide-angle and high-efficiency holographic metasurfaces, Nanoscale **8,** 1588 (2016).

[27] N. M. Estakhri, V. Neder, M. W. Knight, A. Polman, and A. Alù, Visible light, wide-angle graded metasurface for back reflection, Acs Photonics **4,** 228 (2017).

[28] Z.-L. Deng, J. Deng, X. Zhuang, S. Wang, T. Shi, G. P. Wang, Y. Wang, J. Xu, Y. Cao, and X. Wang, *et al.*, Facile metagrating holograms with broadband and extreme angle tolerance, Light Sci. Appl. **7,** 1 (2018).

[29] A. Melnikov, M. Maeder, N. Friedrich, Y. Pozhanka, A. Wollmann, M. Scheffler, S. Oberst, D. Powell, and S. Marburg, Acoustic metamaterial capsule for reduction of stage machinery noise, J. Acoust. Soc. Am. **147,** 1491 (2020).

[30] E. Popov, in *Gratings: Theory and Numeric Applications*, edited by E. Popov (PUP, Aix-Marseille Université, 2012), Chap. 1, p. 3.

[31] D. Maystre, in *Gratings: Theory and Numeric Applications*, edited by E. Popov (PUP, Aix-Marseille Université, 2012), Chap. 2, p. 29.

[32] S. Tretyakov, *Analytical Modeling in Applied Electromagnetics* (Artech House, Norwood, MA, 2003).

[33] J. Liu and N. F. Declercq, Investigation of the origin of acoustic wood anomaly, J. Acoust. Soc. Am. **138,** 1168 (2015).

[34] A. A. Maradudin and I. Simonsen, Rayleigh and Wood anomalies in the diffraction of acoustic waves from the periodically corrugated surface of an elastic medium, Low Temp. Phys. **42,** 354 (2016).

[35] L. Quan, Y. Ra'di, D. L. Sounas, and A. Alù, Maximum Willis coupling in acoustic scatterers, Phys Rev. Lett. **120,** 254301 (2018).

[36] A. Melnikov, Y. K. Chiang, L. Quan, S. Oberst, A. Alù, S. Marburg, and D. Powell, Acoustic meta-atom with experimentally verified maximum Willis coupling, Nat. Commun. **10,** 1 (2019).